Article

Engineering Shape Anisotropy of Fe₃O₄-γ-Fe₂O₃ Hollow Nanoparticles for Magnetic Hyperthermia

Gopal Niraula, Jose A. H. Coaquira, Giorgio Zoppellaro, Bianca M. G. Villar, Flavio Garcia, Andris F. Bakuzis, João P. F. Longo, Mosar C. Rodrigues, Diego Muraca, Ahmad I. Ayesh, Francisco Sávio M. Sinfrônio, Alan S. de Menezes, Gerardo F. Goya, and Surender K. Sharma*

ACCESS | Metrics & More | Article Recommendations | SI Supporting Information

ABSTRACT: The use of microwave-assisted synthesis (in water) of α-Fe₂O₃ nanomaterials followed by their transformation onto iron oxide Fe₃O₄-γ-Fe₂O₃ hollow nanoparticles encoding well-defined sizes and shapes [nanorings (NRs) and nanotubes (NTs)] is henceforth described. The impact of experimental variables such as concentration of reactants, volume of solvent employed, and reaction times/temperatures during the shape-controlled synthesis revealed that the key factor that gated generation of morphologically diverse nanoparticles was associated to the initial concentration of phosphate anions employed in the reactant mixture. All the nanomaterials presented were fully characterized by powder X-ray diffraction, field emission scanning electron microscopy, Fourier transform infrared, Mössbauer spectroscopy, and superconducting quantum interference device (SQUID). The hollow nanoparticles that expressed the most promising magnetic responses, NTs and NRs, were further tested in terms of efficiencies in controlling the magnetic hyperthermia, in view of their possible use for biomedical applications, supported by their excellent viability as screened by *in vitro* cytotoxicity tests. These systems NTs and NRs expressed very good magneto-hyperthermia properties, results that were further validated by micromagnetic simulations. The observed specific absorption rate (SAR) and intrinsic loss power of the NRs and NTs peaked the values of 340 W/g and 2.45 nH m² kg⁻¹ (NRs) and 465 W/g and 3.3 nH m² kg⁻¹ (NTs), respectively, at the maximum clinical field 450 Oe and under a frequency of 107 kHz and are the highest values among those reported so far in the hollow iron-oxide family. The higher SAR in NTs accounts the importance of magnetic shape anisotropy, which is well-predicted by the modified dynamic hysteresis (β-MDH) theoretical model.

KEYWORDS: *Fe₃O₄-γ-Fe₂O₃ hollow nanoparticles, shape anisotropy, magnetic hyperthermia, micromagnetic simulation, modified dynamic hysteresis model*
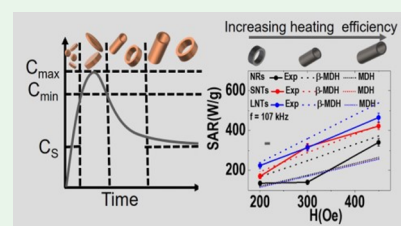
1. INTRODUCTION

The application of magnetic nanoparticles based on various metal-oxides has been studied extensively in the last three decades within the research contexts of medical therapy and diagnostics.[1−6] Ferro/ferrimagnetic magnetite nanoparticles (Fe₃O₄) exhibit low toxicity levels *in vitro* compared to other mixed-metal-oxide systems (e.g. Co/Fe, Mn/Fe, and Ni/Fe),[7−10] but they all suffer from limited chemical stability in physiological solutions (pH values 6.5−7.5 and 9 g/L NaCl), being accompanied with the proclivity to aggregate; these factors limit severely the range of safe concentrations in which these magnetic nanoparticles can be used in clinical application/treatments. Such limitations can be circumvented, on the one hand, by functionalization of the particle surface, using, for example, organic/inorganic and biocompatible canopies, in order to protect the magnetic core from fast degradation (e.g. polyethylene glycol, polyvinylpyrrolidone, chitosan, and SiO₂).[11−14] On the other hand, the surface modification of the magnetic nanoparticle with the organic/inorganic material often results in the decrement of the system magnetic properties expressed in terms of a reduced value of saturation magnetization (M_s); that is, the nonmagnetic part strongly reduces the overall magnetic property of the composite. The partial loss of the magnetic moment is expected to diminish the heating efficiency in magnetic fluid hyperthermia (MFH) application, limiting their potential use in hyperthermia treatments. To address such aggregation, on ferro/ferrimagnetic nanoparticles, the synthesis of hollow particles with magnetic flux-closure-configuration is a unique idea which avoids or at least reduces the dipole−dipole interaction.[15,16] Although magnetism and crystal structures of magnetite (Fe₃O₄) and maghemite (α-Fe₂O₃) are quite similar, the latter form is fully oxidized with all iron in the 3+ state and thus it is more biocompatible and stable against oxidation than
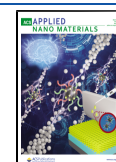
Fe_3O_4. Also, the presence of the Fe^{2+} content of magnetite has deleterious effects *in vitro* due to the generation of reactive oxide species related to Fenton reaction during the cell cycle;[17] thus, it is significant for advancements in the theranostic fields to explore the potentiality of combining shape and phase controlled synthesis of Fe_3O_4 nanoparticles interfaced with γ-Fe_2O_3. Such organization not only should translate into a better heating efficiency of the system but should also be fully stable and biocompatible in the suspension during the MFH process. In the MFH phenomenon, the heating efficiency of the magnetic nanosystem can be enhanced upon altering the effective system anisotropy (K_{eff}), the property that is related to the coercive field (H_C).[18] Effective anisotropy can be interpreted in terms of directional dependence of the magnetic moment (μ), with anisotropic contributions that reflect the material's magneto-crystallinity, shape, nanoparticle's surface disorder, and/or surface corrugation.[19] Structural organization encoding well-defined anisotropy components, such as nanoparticles that adopt a morphology of hollow nanoparticles (HNPs), is seen by many as particularly attractive for achieving better control of the MFH effect.[13,20,21] Therefore, upon altering the phase composition and the form factor (shape and morphology), one can, in principle, fully manipulate the effective anisotropy barrier in the system, which is one direct way to increase the overall heating efficiency during hyperthermia treatments. In the present work, we report results from our studies on the size, that is, from microscale to the nanoscale, and shape-controlled synthesis of hollow α-Fe_2O_3 nanorings (NRs) and nanotubes (NTs) using the microwave-assisted hydrothermal route since it is faster, simpler, and energy-efficient due to the very high rate of microwave heating. We tested several experimental variables such as the reactant concentration, solvent (type and volume), and reaction conditions (time and temperature). After assessing the best synthetic conditions leading to hollow systems, we assembled α-Fe_2O_3 NRs and NTs that were further transformed into Fe_3O_4-γ-Fe_2O_3 materials by reduction−oxidation processes that retained the nanoparticle initial hollow morphology. The presented Fe_3O_4-γ-Fe_2O_3 NT and NR systems were characterized by X-ray diffraction, scanning electron microscopy, Fourier transform infrared spectroscopy (FTIR), Mössbauer spectroscopy, and SQUID magnetometry. The heating efficiency of these systems has been thoroughly analyzed, both experimentally and theoretically, by micromagnetic simulations and the modified dynamic hysteresis model (β-MDH), which is a model applicable in the case of multidomain ferrimagnetic nanoparticles. Taking together all the system properties, we believe that for further advancement in the biomedical-nanotechnology field, and, in particular, in the case of iron oxide systems tailored for hyperthermia treatments, it is key to develop synthetic protocols where the phase composition and anisotropic shape factor become the research key.

2. MATERIALS AND METHODS

2.1. Synthesis of α-Fe_2O_3 and Fe_3O_4-γ-Fe_2O_3 NRs and NTs. The α-Fe_2O_3 NRs and NTs were prepared by a microwave-assisted hydrothermal reaction of iron trichloride ($FeCl_3$) with the addition of sodium dihydrogen phosphate [NaH_2PO_4] and sodium sulphate decahydrate [$Na_2SO_4 \cdot 10H_2O$] as additives to control the shape and morphology. The additives, [NaH_2PO_4] and [$Na_2SO_4 \cdot 10H_2O$], were mixed with 3 mL of distilled water separately and solution of [$FeCl_3$] (73 mL) to obtain a mixture of final volume 76 mL which was then stirred for 15−20 min; the reactant concentrations used for the

nanomaterial assembly were [$FeCl_3$] (0.06 mol L^{-1}), [NaH_2PO_4] (1.8 $\times 10^{-4}$, 3.6×10^{-4}, and 7.2×10^{-4} mol L^{-1}), and [$Na_2SO_4 \cdot 10H_2O$] (1.65×10^{-3} mol L^{-1}). After vigorous stirring for 10 min, the mixtures were transferred into a reaction vessel in a Synth's microwave reactor with an output power of 1000 W. The working cycle of the microwave reactor was set to (i) first step: 20 °C/min rapid heating until two different temperatures were reached, 220 and 240 °C starting from room temperature (RT), and second step (ii): kept for different time (30 and 60 min) at those temperatures. The systems were then allowed to cool down to RT, and the final materials were obtained by centrifugation and were washed with an excess of distilled water and absolute ethanol. Finally, the solids were dried in a vacuum oven at 50 °C. These as-obtained, dried α-Fe_2O_3 NRs and NTs were subsequently reduced by annealing in a furnace at 420 °C for 5 h under a continuous hydrogen/argon gas flow [$H_2/(H_2 + Ar)$ = 4/100]. Then, the system was cooled down to RT under a continuous gas flow to obtain the Fe_3O_4 phase. Finally, the Fe_3O_4 phase was transformed into Fe_3O_4-γ-Fe_2O_3 by oxidation under oxygen flow at 240 °C for 1 h, keeping the desired Fe_3O_4-γ-Fe_2O_3 phase composition while preserving their initial NR and NT morphology. The sulphate and phosphate anions mentioned throughout the manuscript are designated as [SO_4^{2-}] and [PO_4^{3-}], respectively.

2.2. Spectroscopic and Magnetic Characterizations. *2.2.1. X-ray Powder Diffraction.* X-ray powder diffraction of the *as-prepared* materials was obtained from a Bruker diffractometer (Bruker D8 ADVANCE) using Cu $K_{\alpha 1}$ radiation (λ = 1.5406 Å) and a LynxEye linear detector. Data were obtained in the $15° \leq 2\theta \leq 85°$ range with 0.02° step size. The XRD patterns were refined using the Rietveld refinement method through TOPAS [Bruker AXS (2008): TOPAS V4: General profile and structure analysis software for powder diffraction data. User's Manual, Bruker AXS, Karlsruhe, Germany] software.

2.2.2. Electron Microscopy. The morphology of the samples was investigated by using JEOL 7100FT field emission scanning electron microscopy (FESEM, 1.2 nm resolution, operated at 10−30 kV). High-resolution transmission electron microscopy (HRTEM) was performed on a JEOL 2100F instrument using an accelerating voltage of 200 kV.

2.2.3. Fourier Transform Infrared Spectroscopy. A FTIR spectrometer (Bruker, model Tensor 27), equipped with an attenuated total reflectance accessory, was used to identify the functional groups present in the nanoparticles.

2.2.4. Mössbauer Spectroscopy. RT ^{57}Fe Mössbauer spectra were taken in transmission geometry using a constant acceleration-type spectrometer with ^{57}Co in the Rh source also kept at RT. Calibration of the spectra were performed by using an iron foil. The spectra were fitted using NORMOS software.

2.2.5. Magnetometry. Magnetization measurements were carried out on a vibrating sample magnetometer Superconducting Quantum Interference Device (VSM-SQUID) (MPMS Quantum Design) under magnetic fields up to ±70 kOe, at temperatures from 5 to 300 K. Zero-field-cooled (ZFC)/field-cooled (FC) curves were obtained in the temperature range 5−350 K. Both ZFC and FC data were collected while heating the samples, under a cooling field H_{FC} = 50 Oe.

2.2.6. Micromagnetic Simulations. The micromagnetic simulations were performed using the Mumax 3.9 package. In this package, the time evolution of magnetization distribution is obtained by solving the Landau−Liftshitz−Gilbert−Langevin equation (Supporting Information, E1). The magnetic parameters of Fe_3O_4 used in the micromagnetic simulation were as follows: (1) For Fe_3O_4: saturation magnetization M_S = 480 emu/cc, exchange stiffness constant A = 1.2 $\times 10^{-6}$ erg/cm, magneto crystalline anisotropy constant $K_1 = -1.35 \times 10^5$ erg/cc, $K_2 = -0.44 \times 10^5$ erg/cc, and (2) For γ-Fe_2O_3: M_S = 400 emu/cc, exchange stiffness constant $A = 1.1 \times 10^{-6}$ erg/cm, magneto crystalline anisotropy constant $K = 2.3 \times 10^5$ erg/cc[22] The cell size was assumed 5 nm, and the Gilbert damping coefficient was set to α = 0.5.[23,24]

2.2.7. Specific Absorption Rate Measurements. Power absorption measurements were performed using a commercial device (magneT-
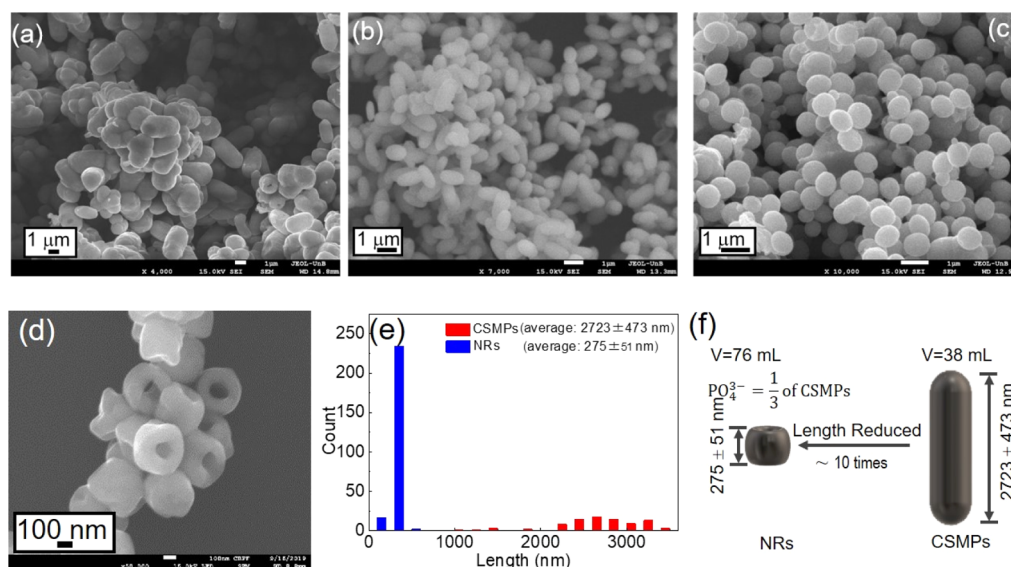
Figure 1. SEM images of α-Fe$_2$O$_3$ products prepared with different concentrations of phosphate anions. Figure 1 (a-d) represents α-Fe$_2$O$_3$ samples including capsule, ellipsoidal, nanodiscs, and nanorings, respectively: (a) [NaH$_2$PO$_4$] = 2.70 × 10^{-4} mol L^{-1}, (b) [NaH$_2$PO$_4$] = 5.40 × 10^{-4} mol L^{-1}, (c) [NaH$_2$PO$_4$] = 4.32 × 10^{-3} mol L^{-1}, (d) NaH$_2$PO$_4$: 1.8 × 10^{-4} mol L^{-1} (t = 30 min and volume of solvent V = 76 mL), (e) comparative distribution of CSMPs (a) and NRs, (d,f) schematic illustration showing the effect of the solvent volume and phosphate anions impacting the morphological parameters (length). For each case (a−d), [FeCl$_3$] = 0.06 M, [Na$_2$SO$_4$·10H$_2$O] = 1.65 × 10^{-3} mol L^{-1}. The temperature employed in the synthesis (T) = 220 °C, time (t) = 60 min, and the volume of solvent of 38 mL for (a−c) while the time and volume solvent are different for (d) as per defined.

herm system, nanoTherics, UK). The heating efficiency of the nanoparticles was measured by a standard calorimetric experimental setup. In these experiments, a vial with the sample is placed into a coil connected to a power generator that controls the amplitude of the AC field inside the coil. An optic fiber temperature sensor was inserted into the vial with the solution to record the temperature. From the initial slope of these temperature versus time curves, the specific absorption rate (SAR) and intrinsic loss power (ILP) can be obtained:

$$\text{SAR} = C\frac{M}{m_{\text{MNP}}}\frac{\mathrm{d}T}{\mathrm{d}t}; \quad \text{and ILP} = \frac{\text{SAR}}{f^2 H}$$

where C is the specific heat capacity of the medium, M is the mass of the fluid, m_{MNP} is the mass of the nanoparticles, "H" is the application of field, and f is its frequency.

2.2.8. Cell Culture Procedures. The murine mammary adenocarcinoma cell line (4T1), murine colorectal carcinoma (CT26), and murine monocyte/macrophage (J774A.1) used in this work were purchased from American Type Culture Collection (USA) and cultured in RPMI supplemented with 10% (v/v) fecal bovine serum (FBS), 100 units penicillin/mL, and 100 mg streptomycin/mL (Gibco, Carlsbad, CA).

Cells were maintained in an incubator under a humidified atmosphere with 5% CO$_2$ at 37 °C. The *in vitro* tests were performed using 96-well microplates, with an initial cell density of 10^4 cell per well. We tested the cytotoxic potential of the two nanoparticle samples, NR and LNT, against three different cell lines: (i) J774A.1; (ii) CT26, and (iii) 4T1. Briefly, cells were seeded in a cell density of 10^4 cells/well in 96-well culture microplates and after 24 h to cell attachment; culture media was replaced by new media containing the nanoparticles (NR and LNT) in different concentrations (0−100 μg/mL). Cells were exposed to nanoparticles for 24 h, and after that, media was removed, the cells were washed with PBS, and the cell viability was then assessed by the MTT assay.

2.2.9. Cell Viability Assay. Cell viability was evaluated by the colorimetric assay method of 3-(4,5-dimethylthiazol-2-yl)-2,5-diphenyl-tetrazolium bromide (MTT, ThermoFisher).[25] After the treatments, the culture medium was replaced by a culture medium with 10% (w/v) MTT. Next, cells were kept in standard culture conditions

for 2.5 h to allow the MTT reaction with the mitochondrial enzymes. Next, the MTT solution was replaced by 100 μL of dimethylsulfoxide (DMSO 99.5%, Sigma-Aldrich) to dissolve cell membranes and extract the formazan crystals produced by the MTT reaction. The optical density formed by solution was measured with a spectrophotometer (λ = 595 nm) and used as an index of cell viability.

3. RESULTS AND DISCUSSION

3.1. Synthesis of α-Fe$_2$O$_3$ and Fe$_3$O$_4$-γ-Fe$_2$O$_3$ NRs and NTs. In this work, we investigate comprehensively the role of phosphate anions in the formation of HNPs and show how their size, shape, and morphology can be obtained by fine tuning the concentration of reactant, volume of solvent employed, time, and reaction temperatures. The experimental variables needed to obtain such shape/morphology defined systems are collected in the Supporting Information (Table S1) with their average sizes. Figure 1a−c shows the so-obtained morphology-based nanoparticles, from microscale to nanoscale, resulting from the analysis of the synthetic variables given in the Supporting Information (Table S1). The morphological evolution from capsule-shape microparticles (CSMPs) and ellipsoidal microrods (EMRs) to a mixture of circular/spherical nanodiscs (NDs/NSs), depended directly on the increasing concentration of phosphate anions present in the reactant mixture; the respective concentrations of phosphate anions used for obtaining CSMPs, EMRs, and NDs/NSs were 2.70 × 10^{-4}, 5.40 × 10^{-4}, and 4.32 × 10^{-3} mol L^{-1}, respectively. When the concentration of phosphate anions was decreased by one-third (i.e., from 2.7 × 10^{-4} mol L^{-1} for CSPMs to 1.8 × 10^{-4} mol L^{-1} for NRs) and the volume of solvent was increased two-fold (~76 mL from the initial ~38 mL at T = 220 °C), a set of NRs reduced in length by almost 1 order of magnitude as observed in the FESEM images (Figure 1d). The size distributions (Figure 1e,f) showed that the length distribution of CSMPs and NRs is easily distinguishable with average lengths of 2723 ± 473 and 275 ± 51 nm, respectively
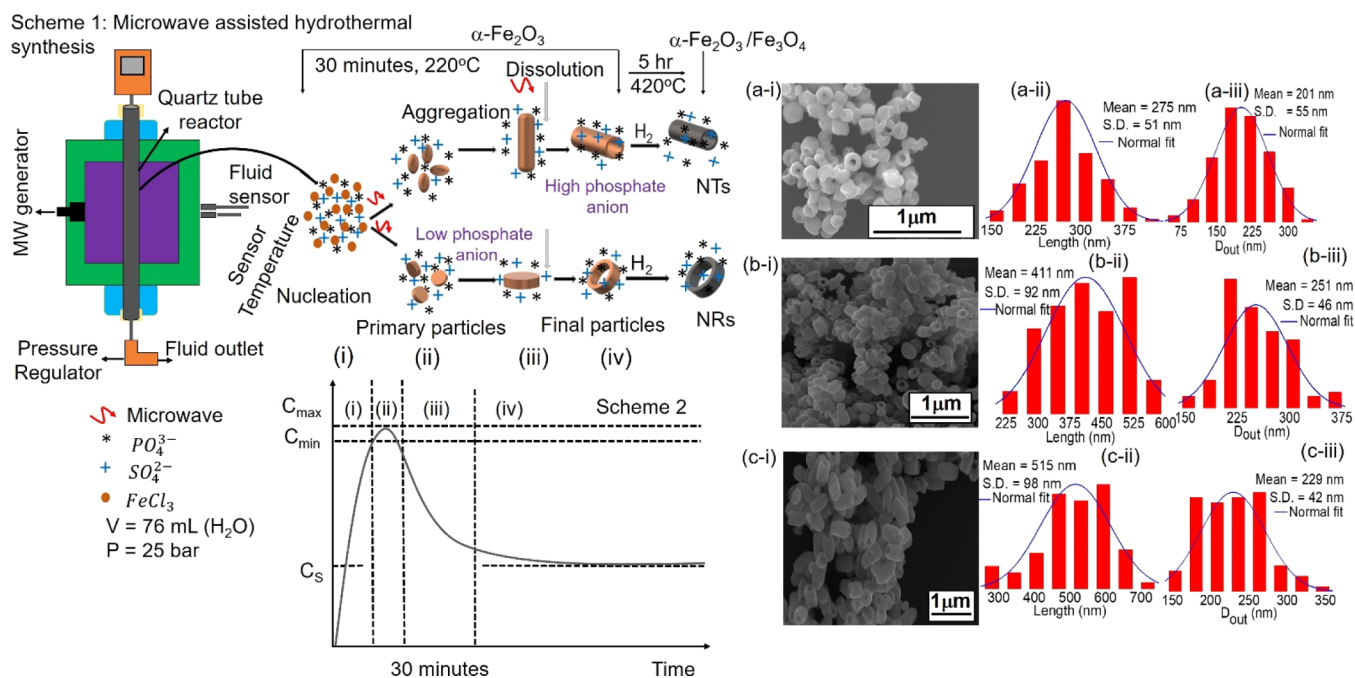
Figure 2. Scheme 1 illustrates the growth process of the diverse iron oxide nanoparticles adopting NTs and NRs morphologies. Scheme 2 is the LaMer's configuration of NPs growth vs time. Panels (a−c) give the SEM images of NRs (Panel a−i), SNTs (Panel b−i), LNTs (Panel c−i), and their respective size distribution analysis. NRs [NaH$_2$PO$_4$]: 1.8×10^{-4} mol L^{-1}, SNTs [NaH$_2$PO$_4$]: 3.6×10^{-4} mol L^{-1} and LNTs [NaH$_2$PO$_4$]: 7.2×10^{-4} mol L^{-1}, [FeCl$_3$]: 0.06 mol L^{-1}, and [Na$_2$SO$_4$·10H$_2$O]: 1.65×10^{-3} mol L^{-1}, synthesis temperature (T) = 220 °C, time (t) = 30 min, and volume of solvent V = 76 mL.

(see also Figure S1 for width distribution in the Supporting Information). The XRD patterns of CSMPs, EMRs, NDs/NSs, and NRs (see Figure S2 and Table S2 in Supporting Information) were refined using the Rietveld method to obtain their structural parameters. These results were consistent with the α-Fe$_2$O$_3$ phase which consists of two different components, that is, grain and crystallite, in a two-crystallite size distribution, and are given in Table S2, with the α-Fe$_2$O$_3$ phase with bigger crystallite size being ∼75−95% and the smaller crystallites ranging from ∼5 to 25%. It is further noticed that the amount of minority phase is similar (i.e. ∼26−29%) for CMPs, EMRs, and NDs/NSs, whereas for NRs, it is only 5%.

Interestingly, the NR structures grew into short NTs (SNTs) and long NTs (LNTs) upon further increase of the concentration of phosphate anions. The FESEM pictures and size distribution analysis of NRs, SNTs, and LNTs are shown in Figure 2a−c. Figure 2 and Scheme 1 illustrate the synthetic steps (nucleation, aggregation, dissolutions, and reductions) involved in the formation of α-Fe$_2$O$_3$ NRs and NTs (SNTs and LNTs) and their reduction into Fe$_3$O$_4$ NRs (l = 275 ± 51 nm; d_{out} = 201 ± 55 nm), SNTs (l = 411 ± 92 nm; d_{out} = 251 ± 45 nm), and LNTs (l = 515 ± 98 nm; d_{out} = 229 ± 42 nm). The role of phosphate and sulphate anions in the formation of NRs to NTs is relatively different. It is reported that the sulphate anions are considered as a growth controller and dissolute agent and has practically no role in shape modification at any concentration;[26] thus, for whole synthesis conditions, the concentration of sulphate anions was fixed. The α-Fe$_2$O$_3$ hollow NRs were obtained using low concentration of phosphate anions; a further increase in the concentration of phosphate anions leads to the growth of SNTs and then LNTs. The schematic growth of NRs toward SNTs and LNTs with increasing concentration of phosphate anions is shown in

Supporting Information Figure S4. The suggested growth mechanism of HNPs (Figure 2 and Scheme 1) was based on local superheating of the aqueous solution that produces numerous "hot spots", boosting the nucleation process.[27,28] Simply, superheating is the metastable state, induced by external or internal effects, in which a liquid is heated to a temperature higher than its boiling point (>100 °C) but without boiling. It can be achieved by heating a homogeneous particle in a clean container and free of nucleation sites in a microwave. Further, "hot spot" formation is due to the localized excessive heat flux on the surface of the nanoparticle during microwave irradiation. The localized overheating and resultant growth of the nonprotective α-Fe$_2$O$_3$ scale considered the primary factors in the initiation of "hot spots". During irradiation, these "hot spot" starts to etch due to localize ionic current generated by high conductivity and polarization of phosphate anions.[29−32] The formation of such "hot spots" on the surface of nanoparticles drives the assembly process of HNPs in a very short span of time. This effect would induce the formation of larger seeds throughout the solution, with rates that depend on the mutual reactant concentrations. The rapid formation of these "hot spots" on the surface of α-Fe$_2$O$_3$ disc/spindle-shaped NPs via irradiation is therefore a unique advantage brought by the microwave synthesis route, which cannot be achieved from any conventional heating methods.

Localized ionic current is generated on these "hot surfaces" of α-Fe$_2$O$_3$ disc/spindle-shaped NPs, due to high conductivity and polarization of phosphate anions during the continuous irradiation process. This localized current in the α-Fe$_2$O$_3$ disc/spindle-shaped NPs drives the preferential dissolution along the crystallographic c-axis (i.e. [001] direction) and favors the formation of a hollow structure in α-Fe$_2$O$_3$ NRs/NTs.[33,34] Finally, the obtained hollow NPs underwent Ostwald ripening, which leads to the final growth of NRs, SNTs, and LNTs upon

increasing the concentration of phosphate anions.[35,36] In the whole synthetic process, sulfate anions thus acted in two steps, (i) during the dissolution process and (ii) during the Ostwald ripening process, while the phosphate anions acted as a shape controller only. The sulphate anions in fact are responsible for the fast dissolution process in the initial seed growth, and then, they control the further growth of the system by modulating Ostwald ripening.[26,33] Overall, the results reveal clearly that the phosphate anions act as a shape controller to induce anisotropic growth and play a crucial role in the formation of HNPs. During the anisotropic growth, the phosphate anions are attributed to the selective adsorption on surfaces parallel to the c-axis, while sulphate anions favor only the dissolution effect due to their coordination with Fe^{3+} cations. The suggested NP formation and their sequential growth mechanism through steps (i−iv) can be visualized with the model pathway proposed by the Extended LaMer's Mechanism (ELM),[37] shown in Scheme 2, which analyzes the growth of nanoparticles with time. Here, C_s is the supersaturation concentration, where monomers are produced and accumulated in solution, but without any formation of nanoparticles; C_{min} and C_{max} are minimum and maximum levels of supersaturation (also called as the critical level of supersaturation) between which the nucleation is energetically favorable. To understand the time dependent growth mechanism of our hollow nanosystem, we have synthesized LNTs at different times, shown in Figure S5, which is analogous to the proposed mechanism Figure 2 Schemes 1 and Scheme 2 collectively. We believe that NRs and SNTs follow a similar mechanism w.r.t. to time. The XRD of α-Fe$_2$O$_3$ NRs, SNTs, and LNTs is given in Figure S6. Then, the Fe$_3$O$_4$ nanoparticles were finally obtained by direct thermal reduction of these α-Fe$_2$O$_3$ NRs, SNTs, and LNTs (see Materials & Method) by preserving their novel morphology. We found that the phosphate anion concentration during the reduction process was the key factor for gated conversion of α-Fe$_2$O$_3$ into Fe$_3$O$_4$. The crystallographic orientation [001] of α-Fe$_2$O$_3$ NRs/NTs transforms into [111] orientation in Fe$_3$O$_4$ NRs/NTs during the thermal reduction process, and this effect is a well-established topotactic transformation.[38] In addition to the topotactic transformation, Becker et al.[39] proposed another scenario potentially responsible for transforming the crystallographic orientation of α-Fe$_2$O$_3$ NTs-[001] into Fe$_3$O$_4$ NTs-[112] and Fe$_3$O$_4$-[113], which is the one driven by formation of twining dislocation.[40] Once Fe$_3$O$_4$ NRs and NTs are obtained, they are partially oxidized in a furnace in the presence of oxygen. Although the reduction process of α-Fe$_2$O$_3$ to Fe$_3$O$_4$ has been well investigated in the literature,[41] the proposed reduction−oxidation pathway, driven by phosphate anions as a key factor, represents a novelty (see Supporting Information for further details).

3.2. Structural Analysis.

After the thermal reduction and oxidation process, we found that the NRs, SNTs, and LNTs consisted of a mixture of the Fe$_3$O$_4$ phase along with γ-Fe$_2$O$_3$ and α-Fe$_2$O$_3$. Figure 3a presents the XRD patterns and their Rietveld refinements for NRs, SNTs, and LNTs. The lattice parameters and phase analysis are given in Table S3. The % of α-Fe$_2$O$_3$ was found to be increased with the concentration of phosphate anions, that is, 3 ± 1% (NRs), 6 ± 1% (SNTs), and 8 ± 1% (LNTs) along with a majority phase of Fe$_3$O$_4$ with a minority of γ-Fe$_2$O$_3$ (∼22 ± 1% of γ-Fe$_2$O$_3$ is present in all samples, i.e., NRs, SNTs, and LNTs, see Table S3). The intense peaks at 2θ = 24 and 33° (marked with * in Figure 3a)
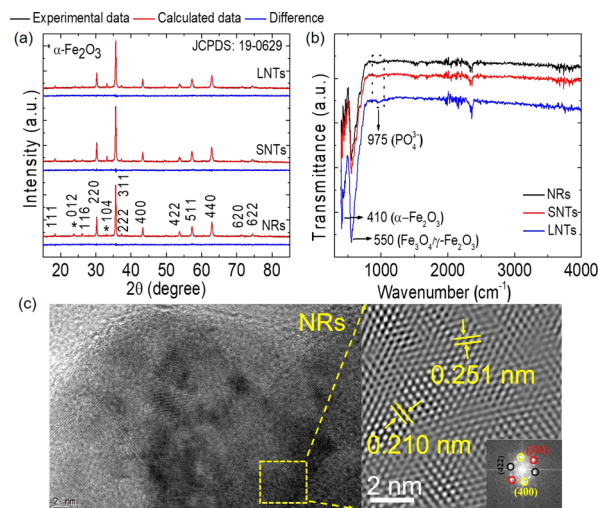
**Figure 3.** (a) Rietveld refining analysis of XRD data and (b) FTIR spectra of α-Fe$_2$O$_3$/Fe$_3$O$_4$-γ-Fe$_2$O$_3$ NRs, SNTs, and LNTs, (c) HRTEM image of Fe$_3$O$_4$-γ-Fe$_2$O$_3$ NRs showing the lattice spacing from indexation. Lower inset of (c) is the fast Fourier transform image.

matched those tabulated for the standard spectra of α-Fe$_2$O$_3$ (JCPDS no. 72-00469), and the broad ones at 2θ = 27.3° corresponded to the diffraction peak (116) of γ-Fe$_2$O$_3$.

The experimental FTIR spectra of α-Fe$_2$O$_3$/Fe$_3$O$_4$/γ-Fe$_2$O$_3$ NRs, SNTs, and LNTs (Figure 3b) obtained in the range of 400−4000 cm^{-1} showed the characteristic vibrational bands from iron oxide (α-Fe$_2$O$_3$/Fe$_3$O$_4$/γ-Fe$_2$O$_3$) NPs between 600 and 400 cm^{-1}. The absorption band at 550 cm^{-1} is assigned to the vibrations of the Fe−O functional group. This band is associated to the stretching and torsional vibration modes of Fe$_3$O$_4$/γ-Fe$_2$O$_3$, whereas the absorption band at 410 cm^{-1} is assigned to the α-Fe$_2$O$_3$ system.[42] The characteristic peak of phosphate/sulphate anions is also detected at 975 cm^{-1}, the value that agrees with the fingerprint known for these functional groups that usually appear in the wavenumber range 950−1200 cm^{-1}.[43] The HRTEM image reveals a lattice spacing of 0.251 and 0.210 nm at the surface Fe$_3$O$_4$-γ-Fe$_2$O$_3$ NRs which agrees well with (311) and (400) planes of the inverse cubic spinel structure[44] as shown in Figure 3c.

3.3. Mössbauer Spectroscopy Analysis.

To better identify the phase composition of the as-prepared iron oxide NPs, RT Mössbauer spectroscopy was performed on α-Fe$_2$O$_3$/Fe$_3$O$_4$/γ-Fe$_2$O$_3$ NR, SNT, and LNT samples. The obtained spectra (Figure 4a−c) could be fitted with five magnetic sites except in the case of NRs, which required only four sextets (see the hyperfine parameters in Table S4 of Supporting Information). The magnetic sextet having hyperfine field B_{hf} = 51.40 and 51.70 T observed in SNTs and LNTs corresponds to the α-Fe$_2$O$_3$ phase (violet solid line in Figure 4b,c), with an estimated population of 7 (±2)% (SNTs) and 8 (±2)% (LNTs), consistent with the XRD analysis. However, this signal was not detected in NRs (Figure 4a), suggesting that the amount of α-Fe$_2$O$_3$ in NRs is below the detection limit of our experimental set up (i.e., less than ∼2 wt %). The spectrum analysis, indicated by navy and purple lines, shows the A (tetrahedral) and B (octahedral) sites of Fe^{3+} cations in γ-Fe$_2$O$_3$. After several fitting attempts with the use of standard parameters[45] of γ-Fe$_2$O$_3$, we found that ∼22% of γ-Fe$_2$O$_3$ is present in all preparations, NRs, SNTs, and LNTs in
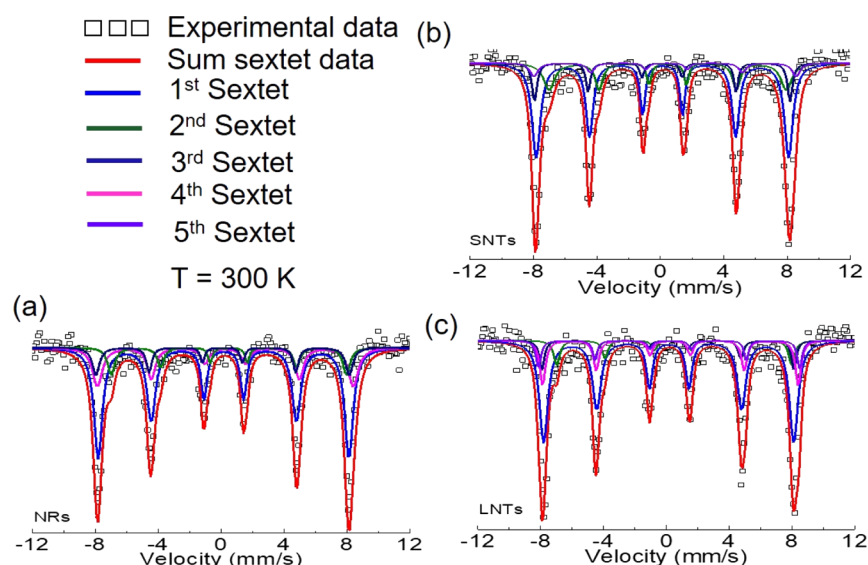
Figure 4. (a−c) Mössbauer spectra of α-Fe$_2$O$_3$/Fe$_3$O$_4$-γ-Fe$_2$O$_3$ NRs, SNTs, and LNTs at 300 K.
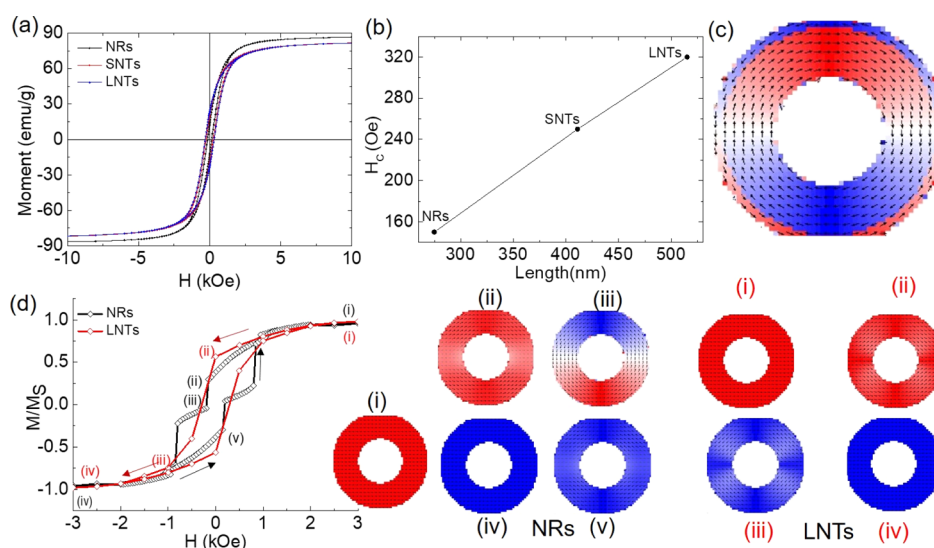
Figure 5. (a) Represents the hysteresis loop at 300 K, (b) coercive field (H_c) dependences on the length of α-Fe$_2$O$_3$/Fe$_3$O$_4$/γ-Fe$_2$O$_3$ NRs, SNTs, and LNTs at 300 K, (c) simulated magnetic ground state of NRs/NTs (upper view), and (d) simulated hysteresis loop of α-Fe$_2$O$_3$/Fe$_3$O$_4$/γ-Fe$_2$O$_3$ NRs and LNTs and their magnetic moment evolution with an applied field.

agreement with XRD data, and the population ratio of A/B equals to 1:1.67 which well agreed with bulk γ-Fe$_2$O$_3$. The result translates into the estimated chemical composition $(Fe^{3+})_A[Fe_{1.67}^{3+}\square_{0.33}]_BO_4$.[45] A similar percentage (~22%) of γ-Fe$_2$O$_3$ in all samples was expected after oxidation of Fe$_3$O$_4$ of 1 h at 240 °C. The fitting analysis, indicated by blue and olive lines in Figure 4a−c, represents the tetrahedral (A-) and octahedral (B-) sites of Fe$_3$O$_4$, respectively. The total population of the Fe$_3$O$_4$ phase contained in A- and B- sites of NRs, SNTs, and LNTs was found to be ~78 (±2), ~72 (±2), and ~70 (±2)%, respectively. The observed population of Fe^{3+} cations residing on A-sites is about 3−4 times larger than those occupying the B-site (Table S4) and, as such, indicates the presence of a large number of cation vacancies (expressed by the symbol) and the defective region on the B-site. The result is a clear signature for formation of nonstoichiometric Fe$_3$O$_4$, which can be represented by the chemical formula Fe$_{3-\delta}$O$_4$, where the factor δ varies

continuously from zero in the case of stoichiometric Fe$_3$O$_4$ up to one-third, for stoichiometric γ-Fe$_2$O$_3$.[45] The higher fraction of Fe^{3+} in the A-site arises from oxidation of Fe^{2+} cations, a process that is enhanced upon increasing the concentration of the phosphate anion, from NRs to LNTs, used during the shape-controlled synthesis. Furthermore, the oxidation process favors the creation of cation vacancies in the B-site and thus drives the Fe$_3$O$_4$ NPs toward the adoption of nonstoichiometric composition. The observed relative composition of Fe$_3$O$_4$ and γ-Fe$_2$O$_3$ from Mössbauer spectroscopy analysis allows us to calculate the approximate value of magnetic saturation, which is ~92 emu/g for NRs, ~88 emu/g for SNTs, and ~87 emu/g for LNTs. Based upon the phase composition analysis, the speculated diameters of Fe$_3$O$_4$-γ-Fe$_2$O$_3$ NRs, SNTs, and LNTs are estimated as 156−45, 196−55, and 179−50 nm, respectively. The calculated magnetization values in the so-prepared nanoparticles have been then assessed by bulk dc magnetization experiments.

3.4. Bulk Magnetic Properties of NRs, SNTs, and LNTs. The dc magnetic data of all samples reflected their ferromagnetic behavior, with saturation magnetization (M_S) of ~88 emu/g for NRs, ~84 emu/g for SNTs, and ~84 emu/g for LNTs. The magnetization trends shown in Figure 5a evidenced that the values from magnetic saturation were slightly lower (about 3−5%) than those predicted by Mössbauer analysis. The observed discrepancy of M_S is due to the presence of the nonstoichiometric Fe_3O_4 phase, which should be slightly larger than those estimated from Mössbauer analysis. We note that M_S decreases from NRs to LNTs, due to an increased % of oxidized Fe_3O_4 (i.e., increase in % of $Fe_{3−\delta}O_4$) owing to higher concentration of phosphate anions. Therefore, the obtained M_S values were greater than those found in the literature of Fe_3O_4 NRs,[16,26] ellipsoidal magnetic particles (EMPs),[5] and NTs.[6]

Figure 5b shows the coercive field H_c that increases with the increasing thickness (or length) of NRs (or NTs), factor that is ascribed to the shape anisotropy contribution of NTs. The shape anisotropy contribution of these NPs can be calculated by using the following eq 1,[44]

$$K_{eff} = K_u + K_s \tag{1}$$

where K_{eff} represents the effective anisotropy constant and K_u and K_s are the magnetocrystalline and shape anisotropy, respectively. Equation 2 gives the anisotropy constant estimation

$$K_s = \left(\pi - \frac{3}{4}N_C\right)M_S^2 \tag{2}$$

with

$$\left[\frac{\rho}{\sqrt{\rho^2 - 1}} \ln(\rho + \sqrt{\rho^2 - 1}) - 1\right] \tag{3}$$

where $\rho = c/a$, being a and c the lengths of the shorter and longer axes of the NPs, respectively. From these expressions, we calculated $K_s = 2.3 \times 10^3$, 3.9×10^3 and 6.0×10^3 erg/cm^3 for NRs, SNTs, and LNTs, respectively, consistent with the micromagnetic simulations (see below). The simulated H_c values give ~190 Oe in NRs and ~295 Oe in NTs. Moreover, Figure 5c depicts the spin configuration, upper view, at the ground state (i.e. $H = 0$) simulated by adjusting the standard parameter of Fe_3O_4 and γ-Fe_2O_3 (as given in Section 2.2.6 micromagnetic simulation).The opposite spin direction (only to identify the core and shell region since has no physical significance here) on the surface indicates the presence of γ-Fe_2O_3 in the surface region. The magnetization reversal process involved in NRs and LNTs is shown in Figure 5d, with the coded red and blue color that indicate M_S in the positive and negative directions, respectively. The drop of H_C from LNTs to NRs and the presence of vortex states (Figure 5d(iii)) in NRs are found in a good agreement with results on similar systems reported by Yang Y. and co-authors in Fe_3O_4 nanodisks[21] and Liu et al.[16] whereas it is completely absent in LNTs, probably due to its tubular morphology.[38] The ZFC and FC (ZFC−FC) curves showing the magnetization versus temperature in the presence/absence of an external magnetic field and are given in the Supporting Information (Figure S7). It was found that no signature of Verwey transition is detected close to 120 K, an effect that indicates the absence of phase transition, from monoclinic to cubic.[46,47] Owing to their higher

effective (shape) anisotropy, the LNTs are expected to express larger SAR values once compared to the NR system. However, the presence of a vortex configuration in NRs should translate into a better heating efficiency, as highlighted in one literature work.[16] Therefore, magnetic hyperthermia experiments were performed in these nanoparticles (NRs, SNTs, and LNTs), and the results are presented and discussed in the following Section 3.5.

3.5. Power Absorption and Heating of NRs and LNTs. Since HNPs with well-defined shapes such as the NRs, SNTs, and LNTs studied here are appealing for biomedical applications due to their flux-closure vortex (e.g. in NRs) and curling (LNTs) configurations that minimize aggregation by dipole−dipole interactions, we studied their heating efficiency for potential MFH applications. Moreover, we added further functional flexibility for MFH applications by coating these HNPs with citric acid as a stabilizing agent (Figure S8), as described elsewhere.[48] We observed that all the coated samples were stable in water for 5 min but then start precipitating/sedimentation. We believe that such stabilization of all the samples was possible due to citrate molecules on the surface in addition to its intrinsic magnetic properties, that is, flux-closure vortex configuration (NRs-Figure 5d) and curling configuration (LNTs-Figure 5d). The SAR measurements were carried out on the water-based colloids with a standard concentration of 1 mg/mL. The applied magnetic field parameters were fixed frequency f = 107 kHz and amplitudes up to H = 35.9 kA/m (450 Gauss), that is, with a product $H \times f \leq 3.8 \times 10^9$ A m^{-1} s^{-1} in such a way to operate below the limit $H \times f \leq 5.1 \times 10^9$ A m^{-1} s^{-1} proposed by Dutz.[49] The SAR values of NRs, SNTs, and LNTs, extracted from the T versus t curves (see Figure S9 in Supporting Information) were measured at increasing field amplitudes H (Figure 6a). The data showed the expected increase of SAR with increasing H but no obvious functional dependence of H.

The highest SAR and ILP values obtained in our samples corresponded to the LNTs, with SAR = 465 W/g and ILP = 3.3 nH m^2 kg^{-1}; these values are among the largest reported for the iron-oxide phases in any nanostructured form under similar f and H_0 conditions. On the other hand, the lowest SPA and ILP values were those from the NR system (SAR = 340 W/g and ILP = 2.45 nH m^2 kg^{-1}). Although the magnetic saturation M_S of NRs was larger than that of LNTs, the heating efficiency appears to be clearly dominated by the shape anisotropy factor. We therefore unveiled, in more details, the role of shape anisotropy on the heating efficiency of hollow NTs in comparison to NRs. For the purpose, we have synthesized a specific sample consisting of size distribution (l = 300 nm; d_{out} = 207 nm; d_{in} = 125 nm) labeled sample "S", having a H_C ~ 155 Oe value very close to H_C ~ 150 Oe of the NRs. The XRD, size distribution, magnetic properties, and heating profile for sample "S" are given in the Supporting Information (Figure S10). The SAR values for "S" sample (Figure 6b) reached 409 W/g at a maximum field amplitude of 35.9 kA/m (450 Oe), which is higher than NRs (SAR = 340 W/g). Although sample "S" has lower M_S and similar H_C, the SAR value of sample "S" is higher than that expressed by NRs, a clear indication that the better anisotropic properties of "S" ($K_s = 2.4 \times 10^3$ erg/cm^3) are translated into a better heating profile. The observed results suggest that the contribution of the shape anisotropy is a key factor to enhance the heating efficiency of HNPs. Interestingly, Figure 6c shows that the heating efficiency is enhanced exponentially as a function of
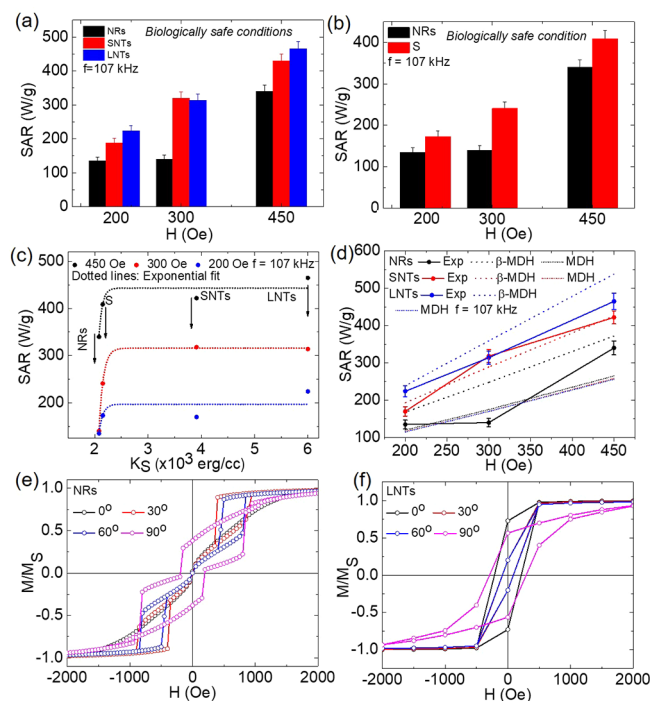
Figure 6. (a) SAR values for α-Fe$_2$O$_3$/Fe$_3$O$_4$-γ-Fe$_2$O$_3$ NRs, SNTs, and LNTs; (b) SAR values for NRs and sample "S"; (c) SAR values for increasing values of shape anisotropies K_S, (d) Comparison of the experimental value of SAR with theoretical prediction based on the β-MDH model, and (e−f) simulated direction dependent hysteresis loop of Fe$_3$O$_4$-γ-Fe$_2$O$_3$ NRs and LNTs.

shape anisotropy, from NRs to LNTs at each field. The exponential fit (dotted lines in Figure 6c) well agreed with the experimental trend. Recently, Tong et al.[50] proposed the use of a modified dynamic hysteresis model (MDH) to obtain SAR values of ferromagnetic iron oxide nanoparticles at the clinically relevant condition (eq 4); the area of hysteresis loss, A, is given by

$$A = 3.53\mu_0 M_S H_{max}(1 - 0.7\kappa) \qquad (4)$$

where μ_0 is the magnetic permeability of vacuum, κ is a nondimensional constant and is negligible for ferrimagnetic materials, M_S is the saturation magnetization, and H_{max} is the maximum applied field. However, we observed that the theoretical SAR values obtained through the proposed MDH model do not satisfactorily reproduce the observed trend for the nanoparticles reported in the present study (see MDH SAR in the Figure 6d). Tong et al.[50] has in fact neglected to include the shape anisotropy factors in their work; thus, we have modified the MDH model by considering the nanoparticle's aspect ratio (β = major axis/minor axis), termed here as the β-MDH model, with mathematical expression given by eq 5

$$A = 3.53\mu_0 M_S H_{max}(1 - 0.7\kappa)\beta \qquad (5)$$

where, β = 1.37, 1.67, 2.23, and 1.44 for NRs, SNTs, LNTs, and sample "S", respectively. Theoretically, the value of "A" (M/M_S, H) obtained using eq 5 allows to calculate the SAR value from eq 6[51,52] as

$$SAR = \frac{M_S f A}{\rho} \times 10^{-7} \text{ W/g} \qquad (6)$$

where ρ is the density of the nanoparticles and f is experimental frequency of the applied field. The calculated SAR values using the modified β-MDH model gives, overall, better adjustment to the trends seen in the experimental data of NRs, SNTs, and LNTs as clearly observed in Figure 6d. However, the β-MDH model still does not account for variables such as the nanoparticle size distribution,[53,54] coercive field,[55] and alignment.[21,51,56] Several studies have demonstrated that the magnetic field gradient usually present in the experimental coils of the magnetic field applicators can induce partial alignment of the free MNPs in the colloid, increasing the absorption power of the colloids up to 2−4 times with respect to the nonoriented nanoparticles.[16,21,56] To assess the impact of this effect on our samples, we performed micromagnetic simulations for the hysteresis losses along different directions of the applied field (Figure 6e,f) for NRs and LNTs to show the possible anisotropic magnetization reversal behavior of NRs and LNTs along different directions.[5] In agreement with previously reported data, a large hysteresis loss was found in the parallel alignment (θ = 90°) for NRs and LNTs, resulting in a higher SAR value.[16,21,56] However, there is no significant difference in the hysteresis loss for both parallel and perpendicular directions of LNTs, as shown in Figure 6f.

Recently, Liu et al.[16] reported the highest SAR (~3050 W/g Fe at 400 kHz and 740 Oe) for magnetic vortex iron oxide nanoparticles, which turned into a much lower value when analyzed at biological relevant conditions. In another work, in iron oxide NTs by Das et al.,[6] the reported SAR values were found to fall at ~ 360 W/g at 800 Oe. Chen et al.[13] reported a significant loss of SAR for γ-Fe$_2$O$_3$@SiO$_2$ NTs (65 W/g) when compared to neat γ-Fe$_2$O$_3$ NTs (~230 W/g) at H = 840 Oe and f = 120 kHz; in the present work, the SAR value of LNTs (465 W/g) shows excellent heating efficiency at low field H = 450 Oe and f ~ 107 kHz; thus, LNTs are the magnetic nanosystem with the highest promises for further studies in living organisms.

The *in vitro* cytotoxicity of two of our systems, namely NRs and LNTs, was assessed through standard MTT viability tests against three different cell lines: 4T1 cells, murine mammary adenocarcinoma cell line; CT26, murine colorectal carcinoma cell line; and J774A.1, a murine monocyte/macrophage cell line. It is important to highlight here that these tests provided evidence of the cytotoxicity of the nanoparticles in different cell lines, therefore providing a more ample basis for potential applications in biomedicine.

The results are presented in Figure 7a and b demonstrated that NR and LNT samples did not produce any significant (p < 0.01) cytotoxicity effects for 4T1 and J774A.1 cells in the range of concentration examined. However, the CT26 cells were found more sensitive than the earlier types when treated with both NR and LNT samples. Conversely, a significant cytotoxic factor was expressed above 2 μg/mL concentration. The viability reduction observed in CT26 cells followed a dose-dependent pattern, indicating the maximum concentration that should be used in this cell type during magneto-hyperthermia applications. Thus, taken together, *in vitro* cytotoxicity experiments reinforce the possibility to implement LNTs in thermal therapy-based applications.

5. CONCLUSIONS

In this work, we have shown the microwave-assisted synthesis of hollow Fe$_3$O$_4$-γ-Fe$_2$O$_3$ nanoparticles encoding well-defined sizes and shapes (NTs and NRs). The obtained iron-oxide
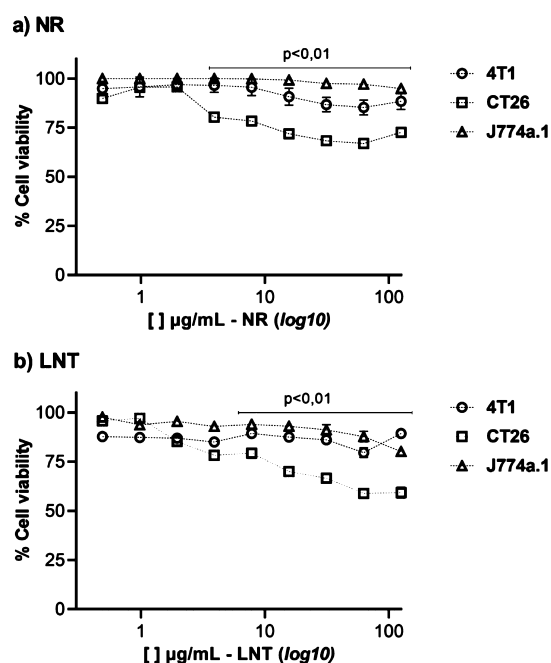
Figure 7. (a) Cell viability tests of NRs and LNTs on 4T1, CT26, and J774 cell lines as a function of increasing (a) NR concentration and (b) LNT concentration. Difference $p < 0.01$ between strains 4T1, J774a.1, and CT26. y-axis refers to untreated cell control and x-axis different sample concentrations in μg/mL. Data presented with standard error in quintuplicates.

samples showed different well-defined geometries (i.e., nanodiscs, NRs, or nanocylinders) depending on the synthesis conditions. The shape-controlled synthesis route was largely influenced by the synthesis parameters such as concentration of reactants, volume of solvent, or reaction time and temperature during the growth process that generated the hollow/capsule tubes, microrods, and nanodiscs, and this was associated to the initial concentration of phosphate anions in the reactants mixture. Indeed, by reducing the concentration of phosphate anions by one-third (and duplicating the solvent volume) in the reactant mixture, the length of the obtained capsule-shaped microparticles (CSMPs) decreased by about 1 order of magnitude (from ~2723 to ~275 nm). Conversely, when the concentration of phosphate anions was increased 4 times the length of NRs, their values were duplicated, leading to the formation of LNTs (length of ~511). The α-Fe$_2$O$_3$ NTs and NRs were then selected as the key nanoparticles to be transformed into HNPs, Fe$_3$O$_4$-γ-Fe$_2$O$_3$, by using reduction-oxidation processes that preserved their initial morphologies. We have assessed the heating efficiency of these morphologically different HNPs for magnetic hyperthermia applications, finding that the LNTs were the best suited for heating, with SAR values up to $\approx$465 W/g for the largest applied fields. These HNPs were found biocompatible and chemically stable. These values are the highest among those reported so far in the hollow ferrimagnetic iron oxide family. Although the magnetic saturation M_S of NRs was found larger than that of LNTs, the heating efficiency appeared to be clearly dominated by the shape anisotropy factor, which was larger in LNTs. Therefore, our work emphasized the relevance of the nanosystem's anisotropy factor, the importance to achieve its control during the bench-synthesis, in a way to optimize formation of nanomaterials for thermal therapy-based applications.

■ ASSOCIATED CONTENT

ⓢ Supporting Information

The Supporting Information is available free of charge at https://pubs.acs.org/doi/10.1021/acsanm.1c00311.

> XRD; SEM; distribution of α-Fe$_2$O$_3$; reduction-oxidation mechanism; phase composition analysis obtained from XRD and Mössbauer analysis; Mössbauer hyperfine parameters; $M_{ZFC/FC}$ versus T measurement; heating profile; and cell viability test (PDF)

■ AUTHOR INFORMATION

Corresponding Author

> **Surender K. Sharma** − *Department of Physics, Federal University of Maranhao, Sao Luis 65080-805, Brazil; Department of Physics, Central University of Punjab, Bathinda 151401, India;* ⓞ orcid.org/0000-0002-6924-7699; Email: surender76@gmail.com

Authors

> **Gopal Niraula** − *Department of Physics, Federal University of Maranhao, Sao Luis 65080-805, Brazil; Laboratory of Magnetic Materials, NFA, Institute of Physics, University of Brasilia, Brasilia 70910-900, Brazil*
>
> **Jose A. H. Coaquira** − *Laboratory of Magnetic Materials, NFA, Institute of Physics, University of Brasilia, Brasilia 70910-900, Brazil*
>
> **Giorgio Zoppellaro** − *Regional Centre of Advanced Technologies and Materials, Faculty of Science, Palacky University in Olomouc, Olomouc 78371, Czech Republic;* ⓞ orcid.org/0000-0003-2304-2564
>
> **Bianca M. G. Villar** − *Brazilian Center for Research in Physics−CBPF, Rio de Janeiro 22290-180, Brazil*
>
> **Flavio Garcia** − *Brazilian Center for Research in Physics−CBPF, Rio de Janeiro 22290-180, Brazil*
>
> **Andris F. Bakuzis** − *Institute of Physics, Federal University of Goias, Goiania 74690-900, Goiás, Brazil*
>
> **João P. F. Longo** − *Department of Genetics & Morphology, Institute of Biological Sciences, University of Brasilia, Brasilia 70910-900, Brazil;* ⓞ orcid.org/0000-0002-5154-7263
>
> **Mosar C. Rodrigues** − *Department of Genetics & Morphology, Institute of Biological Sciences, University of Brasilia, Brasilia 70910-900, Brazil*
>
> **Diego Muraca** − *Institute of Physics "Gleb Wataghin" (IFGW), University of Campinas, Campinas 13083-970, Brazil*
>
> **Ahmad I. Ayesh** − *Center for Sustainable Development, Qatar University, Doha, Qatar; Department of Mathematics, Statistics and Physics, Qatar University, Doha, Qatar;* ⓞ orcid.org/0000-0002-0442-5941
>
> **Francisco Sávio M. Sinfrônio** − *Department of Electrical Engineering, Federal University of Maranhao, Sao Luis 65080-805, Brazil*
>
> **Alan S. de Menezes** − *Department of Physics, Federal University of Maranhao, Sao Luis 65080-805, Brazil*
>
> **Gerardo F. Goya** − *Instituto de Nanociencia y Materiales de Aragón (INMA), Universidad de Zaragoza, Zaragoza 50018, Spain;* ⓞ orcid.org/0000-0003-1558-9279

Complete contact information is available at:
https://pubs.acs.org/10.1021/acsanm.1c00311

Notes

The authors declare no competing financial interest.

◼ REFERENCES

(1) Babes, L.; Denizot, B.; Tanguy, G.; Le Jeune, J. J.; Jallet, P. Synthesis of Iron Oxide Nanoparticles Used as MRI Contrast Agents: A Parametric Study. *J. Colloid Interface Sci.* **1999**, *212*, 474−482.

(2) Wu, W.; He, Q.; Jiang, C. Magnetic Iron Oxide Nanoparticles: Synthesis and Surface Functionalization Strategies. *Nanoscale Res. Lett.* **2008**, *3*, 397−415.

(3) Hurley, K. R.; Ring, H. L.; Etheridge, M.; Zhang, J.; Gao, Z.; Shao, Q.; Klein, N. D.; Szlag, V. M.; Chung, C.; Reineke, T. M.; Garwood, M.; Bischof, J. C.; Haynes, C. L. Predictable Heating and Positive MRI Contrast from a Mesoporous Silica-Coated Iron Oxide Nanoparticle. *Mol Pharm.* **2016**, *13*, 2172.

(4) Ravichandran, M.; Oza, G.; Velumani, S.; Ramirez, J. T.; Garcia-Sierra, F.; Andrade, N. B.; Vera, A.; Leija, L.; Garza-Navarro, M. A. Plasmonic/Magnetic Multifunctional Nanoplatform for Cancer Theranostics. *Sci. Rep.* **2016**, *6*, 34874.

(5) Gao, H.; Zhang, T.; Zhang, Y.; Chen, Y.; Liu, B.; Wu, J.; Liu, X.; Li, Y.; Peng, M.; Zhang, Y.; Xie, G.; Zhao, F.; Fan, H. M. Ellipsoidal Magnetite Nanoparticles: A New Member of the Magnetic-Vortex Nanoparticles Family for Efficient Magnetic Hyperthermia. *J. Mater. Chem. B* **2020**, *8*, 515−522.

(6) Das, R.; Cardarelli, J. A.; Phan, M.-H.; Srikanth, H. Magnetically Tunable Iron Oxide Nanotubes for Multifunctional Biomedical Applications. *J. Alloys Compd.* **2019**, *789*, 323−329.

(7) Lee, J.-H.; Jang, J.-t.; Choi, J.-s.; Moon, S. H.; Noh, S.-h.; Kim, J.-w.; Kim, J.-G.; Kim, I.-S.; Park, K. I.; Cheon, J. Exchange-Coupled Magnetic Nanoparticles for Efficient Heat Induction. *Nat. Nanotechnol.* **2011**, *6*, 418−422.

(8) Horev-Azaria, L.; Baldi, G.; Beno, D.; Bonacchi, D.; Golla-Schindler, U.; Kirkpatrick, J. C.; Kolle, S.; Landsiedel, R.; Maimon, O.; Marche, P. N.; Ponti, J.; Romano, R.; Rossi, F.; Sommer, D.; Uboldi, C.; Unger, R. E.; Villiers, C.; Korenstein, R. Predictive Toxicology of Cobalt Ferrite Nanoparticles: Comparative in-Vitro Study of Different Cellular Models Using Methods of Knowledge Discovery from Data. *Part. Fibre Toxicol.* **2013**, *10*, 32.

(9) Crossgrove, J.; Zheng, W. Manganese Toxicity upon Overexposure. *NMR Biomed.* **2004**, *17*, 544−553.

(10) Kim, D.-H.; Rozhkova, E. A.; Ulasov, I. V.; Bader, S. D.; Rajh, T.; Lesniak, M. S.; Novosad, V. Biofunctionalized Magnetic-Vortex Microdiscs for Targeted Cancer-Cell Destruction. *Nat. Mater.* **2010**, *9*, 165−171.

(11) Pham, X. N.; Nguyen, T. P.; Pham, T. N.; Tran, T. T. N.; Tran, T. V. T. Synthesis and Characterization of Chitosan-Coated Magnetite Nanoparticles and Their Application in Curcumin Drug Delivery. *Adv. Nat. Sci.: Nanosci. Nanotechnol.* **2016**, *7*, 045010.

(12) Tai, M. F.; Lai, C. W.; Abdul Hamid, S. B. Facile Synthesis Polyethylene Glycol Coated Magnetite Nanoparticles for High Colloidal Stability. *J. Nanomater.* **2016**, *2016*, 8612505.

(13) Chen, X.; Klingeler, R.; Kath, M.; El Gendy, A. A.; Cendrowski, K.; Kalenczuk, R. J.; Borowiak-Palen, E. Magnetic Silica Nanotubes: Synthesis, Drug Release, and Feasibility for Magnetic Hyperthermia. *ACS Appl. Mater. Interfaces* **2012**, *4*, 2303−2309.

(14) Zulfiqar; Afzal, S.; Khan, R.; Zeb, T.; Rahman, M. u.; Burhanullah; Ali, S.; Khan, G.; Rahman, Z. u.; Hussain, A. Structural, Optical, Dielectric and Magnetic Properties of PVP Coated Magnetite (Fe3O4) Nanoparticles. *J. Mater. Sci.: Mater. Electron.* **2018**, *29*, 20040−20050.

(15) Li, S. P.; Peyrade, D.; Natali, M.; Lebib, A.; Chen, Y.; Ebels, U.; Buda, L. D.; Ounadjela, K. Flux Closure Structures in Cobalt Rings. *Phys. Rev. Lett.* **2001**, *86*, 1102−1105.

(16) Liu, X. L.; Yang, Y.; Ng, C. T.; Zhao, L. Y.; Zhang, Y.; Bay, B. H.; Fan, H. M.; Ding, J. Magnetic Vortex Nanorings: A New Class of Hyperthermia Agent for Highly Efficient In Vivo Regression of Tumors. *Adv. Mater.* **2015**, *27*, 1939−1944.

(17) Moreno Maldonado, A. C.; Winkler, E. L.; Raineri, M.; Toro Córdova, A.; Rodríguez, L. M.; Troiani, H. E.; Mojica Pisciotti, M. L.; Mansilla, M. V.; Tobia, D.; Nadal, M. S.; Torres, T. E.; De Biasi, E.; Ramos, C. A.; Goya, G. F.; Zysler, R. D.; Lima, E. Free-Radical Formation by the Peroxidase-Like Catalytic Activity of MFe2O4 (M = Fe, Ni, and Mn) Nanoparticles. *J. Phys. Chem. C* **2019**, *123*, 20617−20627.

(18) Stoner, E. C.; Wohlfarth, E. P. A Mechanism of Magnetic Hysteresis in Heterogeneous Alloys. *Philos. Trans. R. Soc., A* **1948**, *240*, 599−642.

(19) Cullity, B. D.; Graham, C. D. Ferrimagnetism. *Introduction to Magnetic Materials*;IEEE Press Wiely, 2009; Chapter 6.

(20) Gutierrez-Guzman, D. F.; Lizardi, L. I.; Otálora, J. A.; Landeros, P. Hyperthermia in Low Aspect-Ratio Magnetic Nanotubes for Biomedical Applications. *Appl. Phys. Lett.* **2017**, *110*, 133702.

(21) Yang, Y.; Liu, X.; Lv, Y.; Herng, T. S.; Xu, X.; Xia, W.; Zhang, T.; Fang, J.; Xiao, W.; Ding, J. Orientation Mediated Enhancement on Magnetic Hyperthermia of Fe_3O_4 Nanodisc. *Adv. Funct. Mater.* **2015**, *25*, 812−820.

(22) Yang, Y.; Liu, X.-L.; Yi, J.-b.; Yang, Y.; Fan, H.-M.; Ding, J. Stable Vortex Magnetite Nanorings Colloid: Micromagnetic Simulation and Experimental Demonstration. *J. Appl. Phys.* **2012**, *111*, 044303.

(23) McMichael, R. D.; Maranville, B. B. Edge Saturation Fields and Dynamic Edge Modes in Ideal and Nonideal Magnetic Film Edges. *Phys. Rev. B: Condens. Matter Mater. Phys.* **2006**, *74*, 024424.

(24) Vaz, C. A. F.; Athanasiou, C.; Bland, J. A. C.; Rowlands, G. Energetics of Magnetic Ring and Disk Elements: Uniform versus Vortex State. *Phys. Rev. B: Condens. Matter Mater. Phys.* **2006**, *73*, 054411.

(25) Coelho, B. C. P.; Siqueira, E. R.; Ombredane, A. S.; Joanitti, G. A.; Chaves, S. B.; Da Silva, S. W.; Chaker, J. A.; Longo, J. P. F.; Azevedo, R. B.; Morais, P. C.; Sousa, M. H. Maghemite-Gold Core-Shell Nanostructures (γ-Fe2O3@Au) Surface-Functionalized with Aluminium Phthalocyanine for Multi-Task Imaging and Therapy. *RSC Adv.* **2017**, *7*, 11223−11232.

(26) Jia, C.-J.; Sun, L.-D.; Luo, F.; Han, X.-D.; Heyderman, L. J.; Yan, Z.-G.; Yan, C.-H.; Zheng, K.; Zhang, Z.; Takano, M.; Hayashi, N.; Eltschka, M.; Kläui, M.; Rüdiger, U.; Kasama, T.; Cervera-Gontard, L.; Dunin-Borkowski, R. E.; Tzvetkov, G.; Raabe, J. Large-Scale Synthesis of Single-Crystalline Iron Oxide Magnetic Nanorings. *J. Am. Chem. Soc.* **2008**, *130*, 16968−16977.

(27) Kim, S.-H.; Lee, S. Y.; Yi, G.-R.; Pine, D. J.; Yang, S.-M. Microwave-Assisted Self-Organization of Colloidal Particles in Confining Aqueous Droplets. *J. Am. Chem. Soc.* **2006**, *128*, 10897−10904.

(28) Hu, X.; Yu, J. C.; Gong, J.; Li, Q.; Li, G. α-Fe2O3 Nanorings Prepared by a Microwave-Assisted Hydrothermal Process and Their Sensing Properties. *Adv. Mater.* **2007**, *19*, 2324−2329.

(29) Topić, M.; Moguš-Milanković, A.; Day, D. E. Study of Polarization Mechanisms in Sodium Iron Phosphate Glasses by Partial Thermally Stimulated Depolarization Current. *J. Non-Cryst. Solids* **2000**, *261*, 146−154.

(30) Pasquini, L.; Wacrenier, O.; Vona, M. L. D.; Knauth, P. Hydration and Ionic Conductivity of Model Cation and Anion-Conducting Ionomers in Buffer Solutions (Phosphate, Acetate, Citrate). *J. Phys. Chem. B* **2018**, *122*, 12009−12016.

(31) Stus, N. V.; Lisnyak, V. V.; Nagornyi, P. G. The crystal structure and ionic conductivity of a novel indium and sodium phosphate Na7(InP2O7)4PO4. *J. Alloys Compd.* **2001**, *314*, 62−66.

(32) Horikoshi, S.; Osawa, A.; Abe, M.; Serpone, N. On the Generation of Hot-Spots by Microwave Electric and Magnetic Fields and Their Impact on a Microwave-Assisted Heterogeneous Reaction in the Presence of Metallic Pd Nanoparticles on an Activated Carbon Support. *J. Phys. Chem. C* **2011**, *115*, 23030−23035.

(33) Jia, C.-J.; Sun, L.-D.; Yan, Z.-G.; You, L.-P.; Luo, F.; Han, X.-D.; Pang, Y.-C.; Zhang, Z.; Yan, C.-H. Single-Crystalline Iron Oxide Nanotubes. *Angew. Chem., Int. Ed.* **2005**, *44*, 4328−4333.

(34) Wu, W.; Xiao, X.; Zhang, S.; Zhou, J.; Fan, L.; Ren, F.; Jiang, C. Large-Scale and Controlled Synthesis of Iron Oxide Magnetic Short Nanotubes: Shape Evolution, Growth Mechanism, and Magnetic Properties. *J. Phys. Chem. C* **2010**, *114*, 16092−16103.

(35) Zhang, R.; Khalizov, A.; Wang, L.; Hu, M.; Xu, W. Nucleation and Growth of Nanoparticles in the Atmosphere. *Chem. Rev.* **2012**, *112*, 1957−2011.

(36) Thanh, N. T. K.; Maclean, N.; Mahiddine, S. Mechanisms of Nucleation and Growth of Nanoparticles in Solution. *Chem. Rev.* **2014**, *114*, 7610−7630.

(37) Vreeland, E. C.; Watt, J.; Schober, G. B.; Hance, B. G.; Austin, M. J.; Price, A. D.; Fellows, B. D.; Monson, T. C.; Hudak, N. S.; Maldonado-Camargo, L.; Bohorquez, A. C.; Rinaldi, C.; Huber, D. L. Enhanced Nanoparticle Size Control by Extending LaMer's Mechanism. *Chem. Mater.* **2015**, *27*, 6059−6066.

(38) Fan, H.-M.; Yi, J.-B.; Yang, Y.; Kho, K.-W.; Tan, H.-R.; Shen, Z.-X.; Ding, J.; Sun, X.-W.; Olivo, M. C.; Feng, Y.-P. Single-Crystalline MFe $_2$ O $_4$ Nanotubes/Nanorings Synthesized by Thermal Transformation Process for Biological Applications. *ACS Nano* **2009**, *3*, 2798−2808.

(39) Becker, P.; Heizmann, J. J.; Baro, R. Relations Topotaxiques Entre Des Cristaux Naturels d'hématite et Le Magnétite Qui En Est Issue Par Réduction à Basse Température. *J. Appl. Crystallogr.* **1977**, *10*, 77−78.

(40) Bursill, L. A.; Withers, R. L. On the Multiple Orientation Relationships between Hematite and Magnetite. *J. Appl. Crystallogr.* **1979**, *12*, 287−294.

(41) Zieliński, J.; Zglinicka, I.; Znak, L.; Kaszkur, Z. Reduction of Fe2O3 with Hydrogen. *Appl. Catal., A* **2010**, *381*, 191−196.

(42) Singh, D.; Gautam, R. K.; Kumar, R.; Shukla, B. K.; Shankar, V.; Krishna, V. Citric Acid Coated Magnetic Nanoparticles: Synthesis, Characterization and Application in Removal of Cd(II) Ions from Aqueous Solution. *J. Water Process Eng.* **2014**, *4*, 233−241.

(43) Elzinga, E. J.; Sparks, D. L. Phosphate Adsorption onto Hematite: An in Situ ATR-FTIR Investigation of the Effects of PH and Loading Level on the Mode of Phosphate Surface Complexation. *J. Colloid Interface Sci.* **2007**, *308*, 53−70.

(44) Cullity, B. D.; Graham, C. D. *Introduction to Magnetic Materials*; John Wiley & Sons, Inc., 2008.

(45) James, M. A.; Hibma, T. NO2-assisted molecular-beam epitaxy of Fe3O4, Fe3− δ O4, and γ− Fe2O3 thin films on MgO (100). *Phys. Rev. B: Condens. Matter Mater. Phys.* **1999**, *60*, 11193−11206.

(46) Shepherd, J. P.; Koenitzer, J. W.; Aragón, R.; Spal/ek, J.; Honig, J. M. Heat Capacity and Entropy of Nonstoichiometric Magnetite Fe3(1-δ)O4: The Thermodynamic Nature of the Verwey Transition. *Phys. Rev. B: Condens. Matter Mater. Phys.* **1991**, *43*, 8461−8471.

(47) Guigue-Millot, N.; Keller, N.; Perriat, P. Evidence for the Verwey Transition in Highly Nonstoichiometric Nanometric Fe-Based Ferrites. *Phys. Rev. B: Condens. Matter Mater. Phys.* **2001**, *64*, 124021−124024.

(48) Li, L.; Mak, K. Y.; Leung, C. W.; Chan, K. Y.; Chan, W. K.; Zhong, W.; Pong, P. W. T. Effect of Synthesis Conditions on the Properties of Citric-Acid Coated Iron Oxide Nanoparticles. *Microelectron. Eng.* **2013**, *110*, 329−334.

(49) Dutz, S.; Hergt, R. Magnetic Nanoparticle Heating and Heat Transfer on a Microscale: Basic Principles, Realities and Physical Limitations of Hyperthermia for Tumour Therapy. *Int. J. Hyperthermia* **2013**, *29*, 790−800.

(50) Tong, S.; Quinto, C. A.; Zhang, L.; Mohindra, P.; Bao, G. Size-Dependent Heating of Magnetic Iron Oxide Nanoparticles. *ACS Nano* **2017**, *11*, 6808−6816.

(51) Usov, N. A.; Nesmeyanov, M. S.; Tarasov, V. P. Magnetic Vortices as Efficient Nano Heaters in Magnetic Nanoparticle Hyperthermia. *Sci. Rep.* **2018**, *8*, 1224.

(52) Carrey, J.; Mehdaoui, B.; Respaud, M. Simple Models for Dynamic Hysteresis Loop Calculations of Magnetic Single-Domain Nanoparticles: Application to Magnetic Hyperthermia Optimization. *J. Appl. Phys.* **2011**, *109*, 083921.

(53) Guibert, C.; Dupuis, V.; Peyre, V.; Fresnais, J. Hyperthermia of Magnetic Nanoparticles: Experimental Study of the Role of Aggregation. *J. Phys. Chem. C* **2015**, *119*, 28148.

(54) Simeonidis, K.; Morales, M. P.; Marciello, M.; Angelakeris, M.; de la Presa, P.; Lazaro-Carrillo, A.; Tabero, A.; Villanueva, A.; Chubykalo-Fesenko, O.; Serantes, D. In-Situ Particles Reorientation during Magnetic Hyperthermia Application: Shape Matters Twice. *Sci. Rep.* **2016**, *6*, 38382.

(55) Zhang, W.; Zuo, X.; Niu, Y.; Wu, C.; Wang, S.; Guan, S.; Silva, S. R. P. Novel Nanoparticles with Cr3+ Substituted Ferrite for Self-Regulating Temperature Hyperthermia. *Nanoscale* **2017**, *9*, 13929−13937.

(56) Das, R.; Alonso, J.; Nemati Porshokouh, Z.; Kalappattil, V.; Torres, D.; Phan, M.-H.; Garaio, E.; García, J. Á.; Sanchez Llamazares, J. L.; Srikanth, H. Tunable High Aspect Ratio Iron Oxide Nanorods for Enhanced Hyperthermia. *J. Phys. Chem. C* **2016**, *120*, 10086−10093.